Experimental and numerical investigation of damage development in embedded rail system under longitudinal force

Wang, Li; Wang, Ping; Chen, Rong; Li, Shaoguang; Li, Zili

DOI
10.1016/j.engfailanal.2020.104590

Publication date
2020

Document Version
Final published version

Published in
Engineering Failure Analysis

Engineering Failure Analysis 114 (2020) 104590

Contents lists available at ScienceDirect

Engineering Failure Analysis

journal homepage: www.elsevier.com/locate/engfailanal

Experimental and numerical investigation of damage development in embedded rail system under longitudinal force

Li Wang[a,b], Ping Wang[a], Rong Chen[a], Shaoguang Li[b], Zili Li[b,*]

[a] Key Laboratory of High-Speed Railway Engineering, Ministry of Education, Southwest Jiaotong University, Chengdu, China
[b] Section of Railway Engineering, Department of Engineering Structures, Faculty of Civil Engineering and Geosciences, Delft University of Technology, Delft, The Netherlands

ARTICLE INFO

Keywords:
Embedded rail system
Damage development
Shear strain
Particle image velocity
Digital image correlation
Finite element analysis

ABSTRACT

Embedded rail system (ERS) is a new type of track structure with many advantages due to its continuous rail support. The rapid development of urban rail transit all over the world renders its application prospect broad. However, the cracks and debonds in ERS present a threat to the traffic safety and a possibility for high maintenance costs. In this work, a longitudinal pushing experiment was designed to explore the damage development process in ERS in order to help structural optimization and performance maintenance. The first order derivative of displacement-longitudinal force curve indicates that the damage process of ERS could be divided into three stages: linear elasticity, damage initiation and damage acceleration stages. The surface deformation of the elastic poured compound (EPC) was analyzed with the particle velocimetry and it is shown that the damage is possibly localized in a small EPC part. Statistics of the absolute displacements of a large number of interrogation areas show that their percentage distribution changes in agreement with the increment of rail displacement, which could be the basis for monitoring of EPC deformation in the breathing zone of continuous welded rail. The analysis of the deformation of EPC from side views, together with the qualitative analysis with finite element method, reveals that the large shear strain of rubber strip and the intense shear strain of EPC at rail foot are the main causes of damage initiation and growth in ERS under longitudinal force.

1. Introduction

Embedded rail system (ERS) is distinguished from traditional track structures by its special rail support. Rather than discretely supported by sleepers, the rail in ERS is continuously supported by rubber strip and elastic poured compound (EPC) which surrounds almost the entire rail except the rail head (see Section 2.1: the details of ERS). ERS thus has advantages in providing obstacle-free surface for crossing traffic, the absence of dynamic forces due to secondary bending between single rail supports [1,2], as well as the reduction of noise radiation and maintenance [1]. The application of continuous support of ERS can be found from tram track to high-speed railway [1].

However, cracks can happen at the interfaces between EPC and the concrete groove or the rail, as well as in EPC itself, as shown in Fig. 1. At the interfaces, cracks can initiate, grow and finally lead to debonds. Debonds are a more detrimental form of damages, and they can extend with cracks along the interfaces.

* Corresponding author at: Section of Railway Engineering, Delft University of Technology, Stevinweg 1, 2628CN, Delft, The Netherlands.
E-mail addresses: l.wang-7@tudelft.nl (L. Wang), wping@home.swjtu.edu.cn (P. Wang), chenrong@home.swjtu.edu.cn (R. Chen), s.li-1@tudelft.nl (S. Li), z.li@tudelft.nl (Z. Li).

https://doi.org/10.1016/j.engfailanal.2020.104590
Received 26 January 2020; Received in revised form 12 May 2020; Accepted 13 May 2020
Available online 16 May 2020
1350-6307/

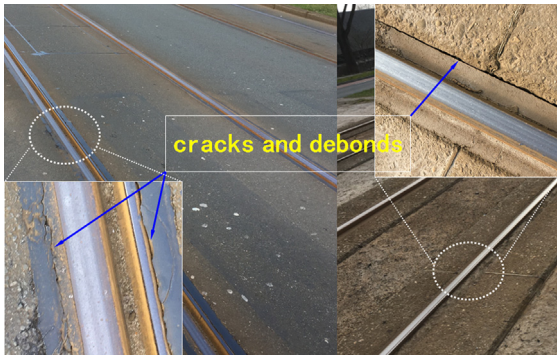

Fig. 1. Cracks and debonds in ERS.

The cracks occur frequently, making ERS difficult to reach to its expected long service life. It is not easy to observe where the cracks start since the rail is buried in EPC in concrete groove. To detect the subsurface cracks is time consuming and it also does not solve the root problem, because after local maintenance like EPC replacement, the cracks can still occur before long.

Cracks often indicate insufficient material strength or sub-optional structure design. Therefore, numerical techniques and laboratorial experiments were employed to optimize the structure design and the material properties [3]. Construction craft was also improved. The concrete groove was brushed and then painted with a primer designed to enhance the adhesive strength between the groove and EPC [2]. The situation is much better but, unfortunately, cracks can still happen commonly in various types of ERS. Thus, a further understanding is needed of the embedded rail structure and its damage process.

The development of cracks has attracted the interests of many researchers. Fatigue crack initiation and growth in rail [4–7], fracture instabilities at crack tips of hyperelastic materials like rubber [8–9], as well as fracture mechanics analysis of cracks in plain and reinforced concrete [10–12] are all fascinating research topics. The rubber-to-metal bond failure was also studied [13]. However, little scientific research on damage development of composite structures like ERS has been reported. ERS involves at least three types of materials and multiple complex bond conditions not only at the interfaces between EPC and rail but also at the interfaces between EPC and concrete groove, which makes the study of ERS failure much more difficult and complicated.

The degradation situation of ERS is quite different from that of traditional railway track, especially in the following two aspects. On the one hand, the internal damage of ERS is not easy to be noticed because of the encapsulation of rail by EPC. It is possible that multiple cracks have already occurred inside but nothing unusual could be seen from the surface of ERS, which poses a risk to the traffic safety. On the other hand, there is no need to pay too much attention to some tiny local crack inside EPC or at the interfaces because the constraint of rail from EPC is continuous and all-around. That is to say, a critical length of damage exists and the track is still operationally safe and economical if the length of damage is smaller than the critical length. For this, the process of damage development in ERS should be well-understood for a cost efficient maintenance.

ERS is exposed to multiple complicated loads, such as axle loads, temperature forces, and subgrade settlements. The loads in the longitudinal direction are more likely to cause damage in ERS. The braking force, and the movement of long rail in breathing zone of continuous welded rail (CWR) as temperature rises and falls are all possible to disturb the EPC and then result in damage. The loads in the other two directions are relatively less critical because the displacement of rail in the vertical or lateral direction is more limited due to the constraints from the concrete groove.

To reduce the construction time, ERS is usually designed as slab structure with precast slabs which can be produced in factory. However, the gaps between the slabs become the naturally vulnerable parts, because the continuous rail support is interrupted at the gaps. This discontinuity would lead to weakening and premature failure of ERS under the effects of train loads, subgrade settlements and the interaction between bridge and rail.

In this paper, a laboratory experiment was designed to explore the initiation and growth process of damage in ERS under longitudinal force. In the experiment, two 600 mm specimens were prepared. Each of them contained the main characteristics of ERS and was pushed longitudinally via a load cell. The rail displacement was measured by displacement meters and the deformation of EPC was captured by cameras from top view and side views, see Section 2. Then, in Section 3, the test results were analyzed to identify different stages of the damage process and the deformation feature of EPC. After that, in Section 4, a finite element ERS model was built to simulate the experiment so as to get a better understanding of the damage process of ERS. Finally, in Section 5, conclusions were drawn and the work need to be done in the future was put forward.

2. Design of the experiments

2.1. Details of ERS

ERS commonly contains rail, EPC, rubber strip, levelling shim and precast blocks for noise reduction, as well as a concrete groove to enclose the components above, as shown in Fig. 2.

The rail can be standard rail or grooved rail, used to bear and transmit the loads from the train. Rubber strip provides the vertical

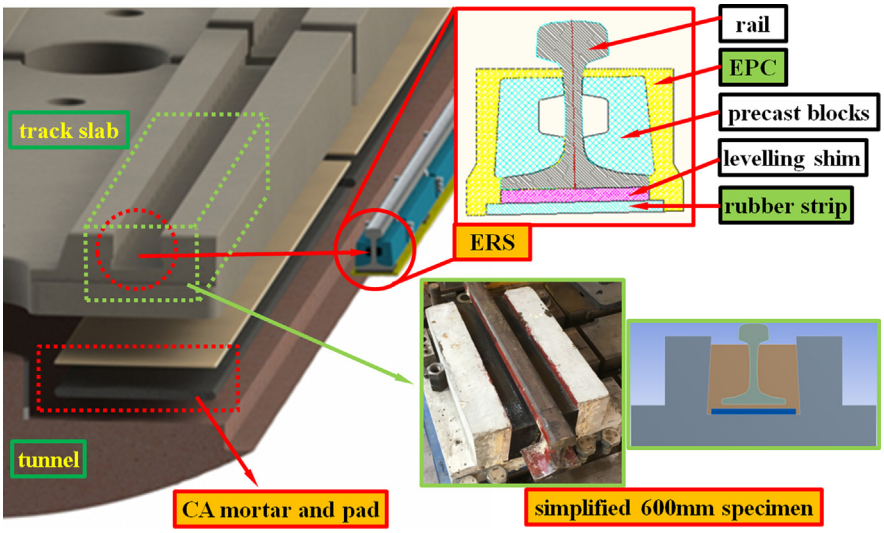

Fig. 2. Details of ERS and simplified specimen used in experiment.

elasticity. Precast blocks were glued strongly with the rail and then together placed into the concrete groove. The precast blocks can reduce the amount of EPC and also reduce the noise from rail vibration. The variable thickness of the levelling shims can adjust the rail elevation where needed. Levelling shims are made of the same materials as EPC in order to provide uniform continuous support for the rail. After adjustment, the rail will be stress free before the EPC is poured into the groove. When the EPC fills in all the void space, and solidifies, the spatial constraint on the rail is formed.

The shape of the cross section of concrete groove is usually not rectangular but can be trapezoidal or with a bulge at the bottom corner, which can make the bottom wider than the top, so as to constrain the rail against uplift. In this study, the wall of the concrete groove is inclined, so the shape is a trapezoid.

Some assumptions are made. Firstly, the interfaces between EPC and precast blocks will never break and also precast blocks will be bonded perfectly with the rail. Actually, there is a tendency to do without the precast blocks because they have intricate construction procedures but their noise reduction and cost saving effects are limited. Thus, the places of precast blocks are filled with EPC in this study. Secondly, the levelling shims do not affect the damage initiation and growth. This is out of the consideration that, in construction, the levelling shims are not placed regularly but inserted randomly to where there is a need for geometric alignment of rails.

Thus, the test specimen contains only the rail, EPC, rubber strip and concrete groove, as is shown in the simplified 600 mm specimen in Fig. 2.

2.2. Setup of the experiment

2.2.1. Particle image velocimetry

Particle image velocimetry (PIV) has long been used for measuring instantaneous velocity and the related properties in fluids which is seeded with tracer particles [14–16]. Its concept of using cross-correlation to detect shifts in datasets, also known as digital image correlation (DIC), has increasingly been becoming popular in many research fields like geomechanics [17], solid mechanics [18–20] and railway engineering [21], especially in micro- and nano-scale mechanical testing applications [22–23]. Its measurement principle is illustrated in Fig. 3.

As shown in Fig. 3, the interesting part of a surface is chosen as a target area. Images of the target area are then divided into small subsections called interrogation areas which are cross-correlated with each other, pixel by pixel. The correlation produces a signal peak, identifying the common particle displacement. The accurate displacement vectors are thus achieved by sub-pixel interpolation.

Many freely available softwares can help to do the calculation if the images of target area are prepared, such as MatPIV [24], OpenPIV [25] and PIVlab [26–27].

2.2.2. Experimental procedure

The setup is shown in Fig. 4. The concrete groove was fixed to the rigid floor and the rail was pushed at one end by a hydraulic jack. The hydraulic jack provided gradually increasing loads. At the opposite end of the rail, three displacement meters recorded the longitudinal displacements of the rail from rail head and rail foot sides. Each time when the longitudinal load was stabilized after a designed increment, the top and two side views of the specimen reflecting the real-time deformation of EPC were captured by three cameras. Images from top view would be used to explore the deformation of EPC, while the images from side views help capture and understand the damage process.

Two specimens were tested to verify the repeatability. Each specimen was loaded five times. From the 1st to the 4th time, the

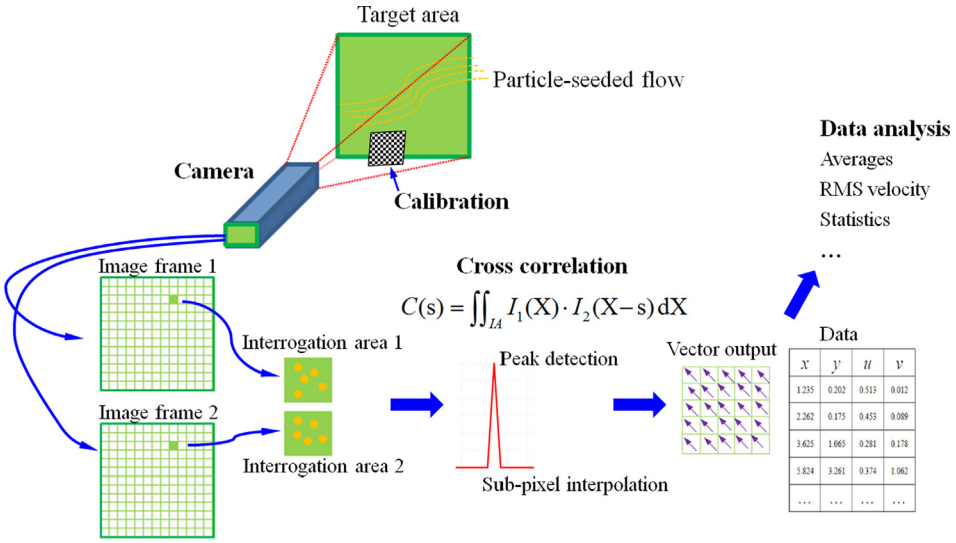

Fig. 3. Measurement principle of PIV.

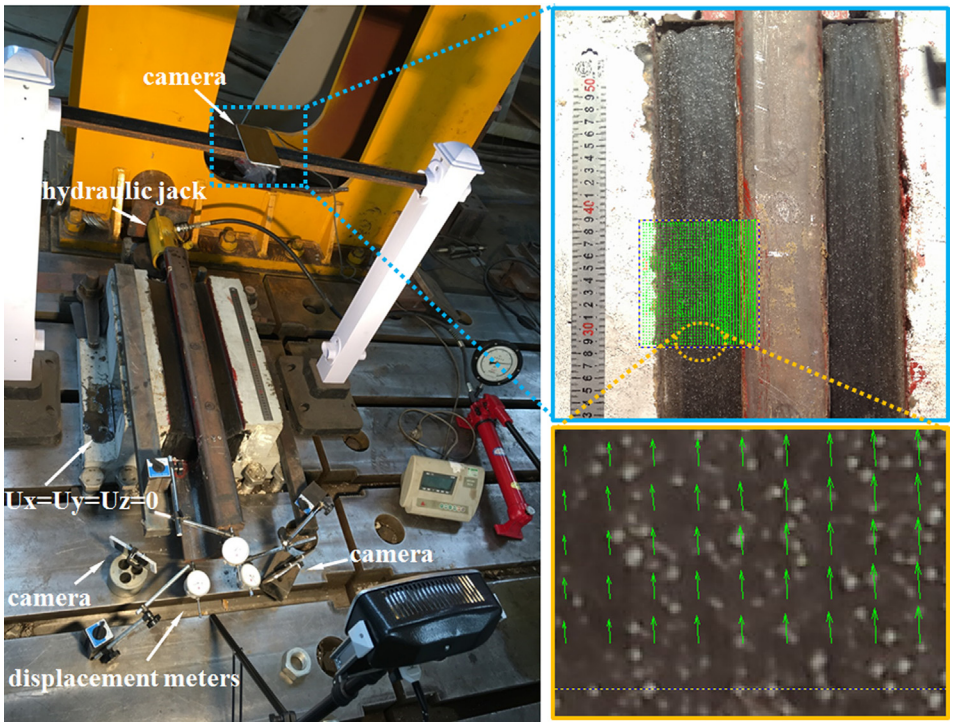

Fig. 4. Experiment setup.

loading was stopped when the rail displacement was about 4 mm, while at the 5th time, the load would be applied until that crack or debond between the EPC and the rail or the concrete groove is obvious in top view to naked eyes. The first four loadings can make sure that there was no significant original damage in the specimen if the load–displacement curves show acceptable repeatability. Emphasis would be put on the 5th load–displacement curve which indicates the damage rule of ERS under longitudinal force.

3. Results and discussion

3.1. Three stages in damage process

Measured load–displacement relationships for the two specimens are shown in Fig. 5. Loadings within the 4 mm limit rail

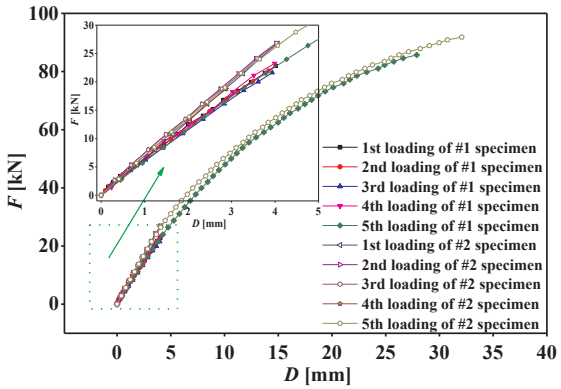

Fig. 5. Load-displacement curves of the two specimens (F – longitudinal force; D – rail displacement).

displacement show great repeatability, which indicates that the two specimens were well prepared without significant original damage. The two specimens also behaved very similarly in the 5th loading. The load–displacement curve is linear when the displacement is less than 5 mm but gradually bends down as displacement grows. The bent load–displacement curve means decreasing longitudinal stiffness of the ERS. If the stiffness of a structure is decreasing, it is most probably that damage is developing in the structure. But of course, possible nonlinear material property of the EPC could also contribute to reduction in stiffness.

The two 5th load–displacement curves go very closely to each other and the difference is only at the end where the larger force and displacement broke the #2 specimen. Because of the very similar loading process, the discussion will take the situation of #1 specimen for example.

To show more details of the rail displacement, the displacement gradient by force, $\frac{\partial D}{\partial F}$, was derived as depicted in Fig. 6. The displacement gradient can tell how the rail displacement change as the force grows. Each point in the displacement gradient curve indicates how much displacement per newton occurs when the force increases. To know how fast the displacement changes with force, the second order derivative of displacement by force, i. e. $\frac{\partial^2 D}{\partial F^2}$, should be examined.

If $\frac{\partial^2 D}{\partial F^2} > 0$, it means the change of displacement becomes faster, e.g. when the force changes from 77.2 kN to 79.8 kN in Fig. 6.

If $\frac{\partial^2 D}{\partial F^2} = 0$, it means the change of displacement is stable, e.g. when the force changes from 0 to 20.0 kN.

If $\frac{\partial^2 D}{\partial F^2} < 0$, it means the change of displacement becomes slower, e.g. when the force changes from 79.8 kN to 82.3 kN. But note that, even if the change of displacement becomes slower, the displacement can still be increasing.

From the trend of displacement gradient $\frac{\partial D}{\partial F}$, the whole loading process could be approximately divided into three stages, as illustrated in Fig. 6. In stage I, with rail displacement from 0 to about 4 mm, the displacement gradient is stable which represents linear material property with no damage. It is a safe period and ERS can work well due to limited component deformation. In stage II, with rail displacement from 4 mm to 15 mm, the displacement gradient fluctuates gently. Some debonding or material damage may be happening during this stage. It is a damage initiation period. In stage III, with rail displacement from 15 mm till the end of loading, the displacement gradient fluctuates dramatically and finally obvious damage could be observed from the surface of EPC. Much damage in ERS should have been produced during this stage and it is an accelerated damage period.

This division into three stages is also applicable to specimen #2, as is shown in Fig. 7.

Though during stage I, ERS does not seem to show any damage, it still contributes to the following two stages, so stage I can still be considered as part of the damage process.

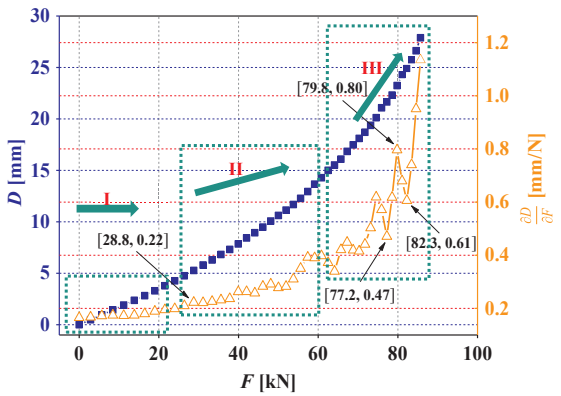

Fig. 6. Rail displacement D (blue ■) vs. its gradient $\frac{\partial D}{\partial F}$ (orange △).

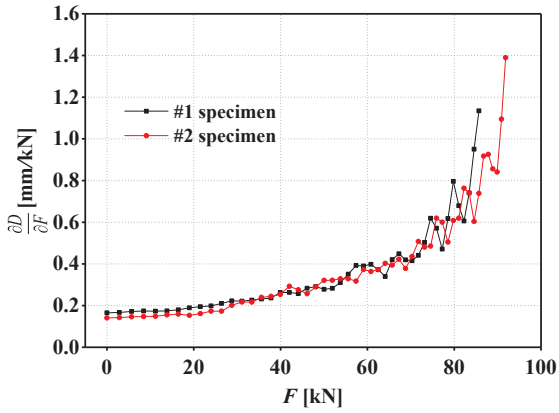

Fig. 7. Displacement gradient of the two specimen.

3.2. Deformation of EPC from the top view

3.2.1. Result of PIV calculation

As is mentioned above, each time when a larger force F was applied, the top view of the specimen was captured for PIV analysis. The focus was on the surface deformation of EPC. Due to the symmetry of the specimen, only half of the EPC surface was considered as the target area, as illustrated in Fig. 8(a). Actually, the image in Fig. 8(a) is the last one captured in the experiment, in which the first debonding in top view of the EPC surface can be observed, as is shown in the zoom-in on the left side of Fig. 8(a).

The size of each pixel in the pictures captured in the experiment was about 0.2646 mm^2. Considering the balance between calculation accuracy and time, the target area in PIV analysis was meshed by 1 mm × 1 mm. Thus, the total number of interrogation areas was about 38400. As shown in the zoom-in on the right side of Fig. 8(a), each green arrow represents the displacement vector of an interrogation area [27]. From the concrete groove side to the rail side, the green arrows grow in length, because the concrete groove was fixed with no displacement and the rail was pushed longitudinally with the maximum displacement. Also, the green arrows are almost all parallel to each other, indicating that, generally, the shear deformation of surface EPC was quite homogeneous and uniform.

For quantitative analysis, the green arrows in Fig. 8(a) are transformed into points, as shown in Fig. 8(b), in which each point P represents the displacement vector $\vec{I_P}$ of an interrogation area during one load increment [27].

$$\vec{I_P} = \vec{I_P}(u_P, v_P) \tag{1}$$

and $|\vec{I_P}|$ is its magnitude

$$|\vec{I_P}| = \sqrt{u_P^2 + v_P^2} \tag{2}$$

where u_P and v_P are the longitudinal and lateral displacement, respectively.

The distribution of the points in one load increment can be quite different from that in the other load increments. Fig. 8(b) shows the distributions from three consecutive load increments for example. Also, it can be seen that the distribution of the points in each load increment is not absolutely homogeneous, reflecting the inhomogeneous strain of EPC which is hard to see from the distribution of green arrows in Fig. 8(a). To detect a subtle variation, in one load increment or between different load increments, statistical analysis needs to be conducted, as will be shown below in Section 3.2.2.

Additionally, it is possible that the linear regression line is inclined (the green line in Fig. 8(b)), because it is difficult to put the camera in a position that it can have a view with boundaries strictly paralleling to the rail direction. But this doesn't matter, we can get the inclination θ (about 2.24° in Fig. 8(b)) and we can also compensate this by a statistical analysis below.

3.2.2. Statistical analysis of displacement vectors

Owing to the large number of interrogation areas, it is possible to perform a statistical analysis according to the magnitudes of the displacement vectors, i.e. the absolute displacements of the interrogation areas.

As shown in Fig. 8(b), in each load increment, the absolute displacement of an interrogation area varied from 0 to about 1.0 mm. Divide [0.0, 1.0] into 50 uniform intervals of width 0.02 mm, any point in Fig. 8(b) will fall into one of these intervals. For example, the point P(0.4,0.01) belongs to the interval [0.4 mm, 0.42 mm). In some other load increments, some more intervals are needed to accept the points with larger absolute displacements.

According to experience, the interval width 0.02 mm is suitable to form a clear histogram. The percentage distributions of the absolute displacements of interrogation areas in the last seven load increments are shown in Fig. 9.

In Fig. 9, each bar represents the percentage of a certain absolute displacement. For example, in Fig. 9(a), in the load increment from 77.2 kN to 78.5 kN (see the black bars), of all the interrogation areas (about 38,400 areas), about 4% has an absolute

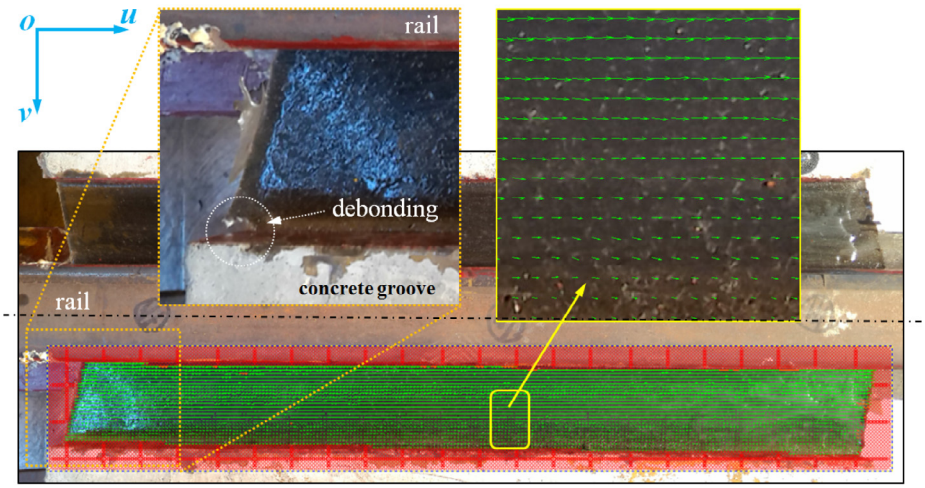

(a) The last moment image (top view, specimen #1) with lower half EPC meshed into grid.

(Zoom-in on the left side: debonding between EPC and concrete groove;

Zoom-in on the right side: displacement vectors of interrogation areas)

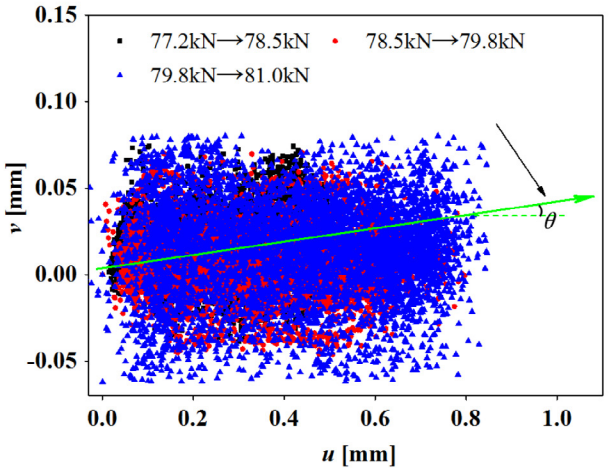

(b) Displacement vectors of the interrogation areas from 3 consecutive load increments

(*u* and *v* are longitudinal and lateral displacement, respectively)

Fig. 8. PIV analysis of EPC surface and displacement vectors output.

displacement ($|\vec{I_P}|$) of 0.2 mm.

It can be seen from Fig. 9 that the percentage distribution in one load increment could be quite different from that in another load increment, even if the magnitude of each load increment was almost the same, i.e. 1.2 kN.

This percentage distribution would be probably related to the rail displacement, i.e. *D*, because the deformation of EPC was caused by the rail movement. The more the rail moved, the larger deformation the EPC would have.

When the force is applied from $F_{i\text{-}1}$ to F_i , the rail displacement recorded by displacement meters comes from $D_{i\text{-}1}$ to D_i, then

$$\Delta D_i = D_i - D_{i-1} \tag{3}$$

where $F_0 = 0$, $D_0 = 0$, $i = 1,2,3,\ldots$

In Fig. 9(a), comparing with load increment from 77.2 kN to 78.5 kN, the load increment from 78.5 kN to 79.8 kN makes a wider range of percentage distribution with absolute displacement from 0 to 0.8 mm. Especially in the range of 0.5 mm to 0.8 mm, there are only red bars but nearly no black bars. It is in accordance with the variation trend of ΔD in the inset of Fig. 9(a), where the red open square is higher than the black open square. That is to say, if the bars spread over a larger percentage distribution range, the corresponding ΔD will be larger.

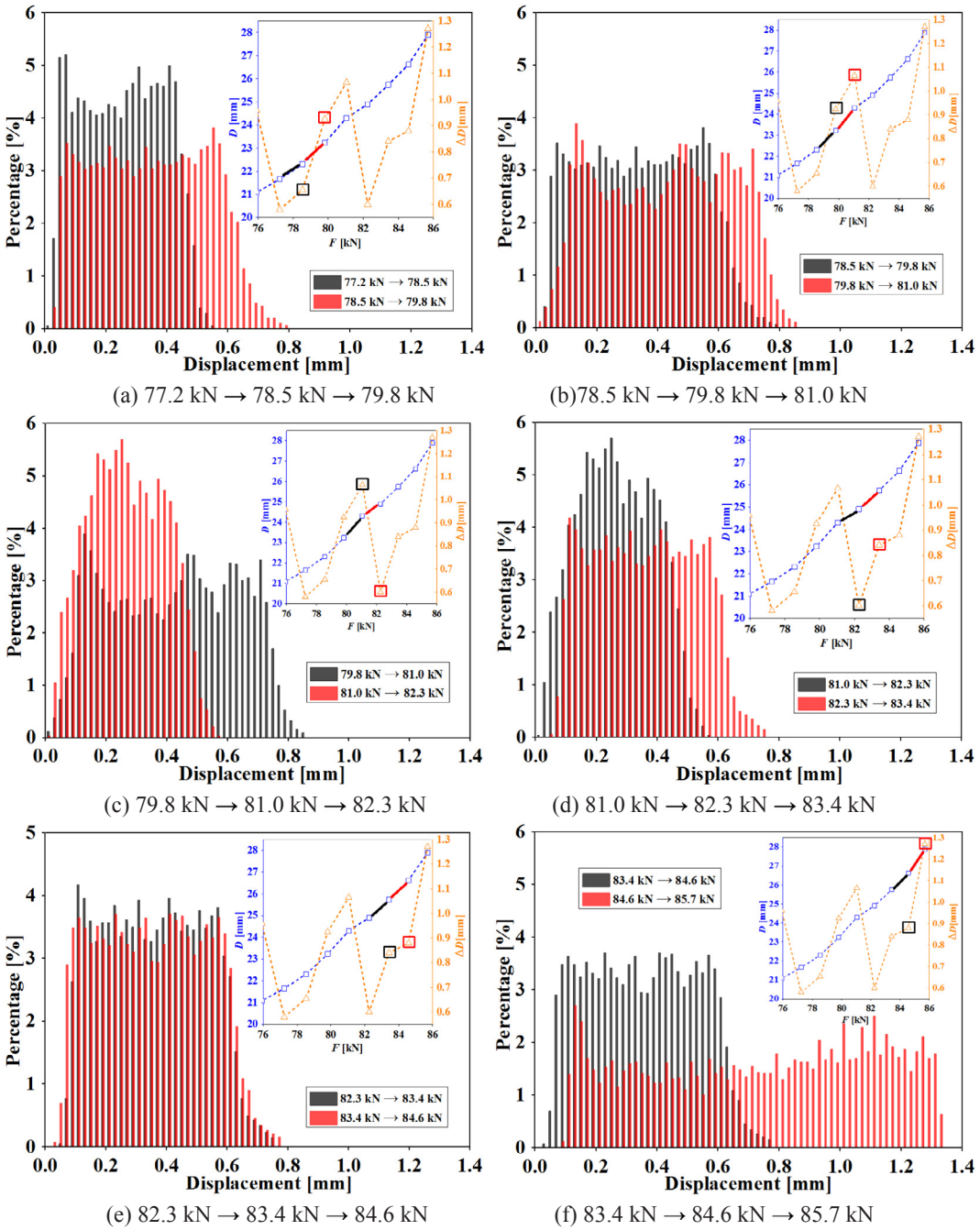

Fig. 9. Percentage distributions of the absolute displacements in the last 7 load increments.

In the inset of Fig. 9(b), the red open square stands again higher than the black open square, that is why the red bars spread over a relatively larger displacement range.

Fig. 9(c), (d) and (e) confirm this rule.

It is worth mentioning that, in Fig. 9(f), the red bars spread over much wider displacement range including 0.8 mm to 1.3 mm, which means unusual surface deformation happened when the force was applied from 84.6 kN to 85.7 kN. This unusual surface deformation could be explained as the debonding between EPC and the rail or between EPC and the concrete groove, as well as the possible EPC damage itself.

From the observations in the experiment, this unusual surface deformation was confirmed to be caused by the debonding between EPC and the concrete groove at the left corner, as shown in the zoom-in on the left side of Fig. 8(a).

Additionally, ΔD is somewhat different from $\frac{\partial D}{\partial F}$, even if they have similar variation trend, as depicted in Fig. 10.

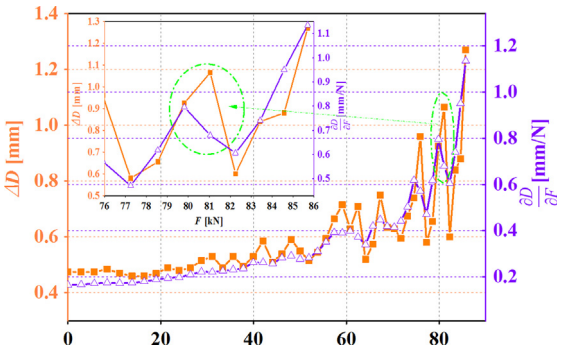

Fig. 10. Variation trend of ΔD (orange ■) vs. that of $\frac{\partial D}{\partial F}$ (violet △).

Moreover, from Fig. 9 and Fig. 10, it can be found that the variation of the percentage distributions in the last seven load increments is more related to ΔD than $\frac{\partial D}{\partial F}$. In Fig. 9(b), the red bars spread wider than the black bars, thus the red open square (F = 81.0 kN) should stand higher than the black open square (F = 79.8 kN), as is shown in the inset in Fig. 9(b). Yet in the inset of Fig. 10, it can be seen that, in the load increment from 79.8 kN to 81.0 kN, the violet open triangle line ($\frac{\partial D}{\partial F}$-$F$) is going down, rather than going up like orange solid square line (ΔD-F) .

Thus, the surface deformation of EPC is more related to rail displacement increment rather than its gradient (by force). This is an important feature to make EPC damage assessment be conducted possibly without longitudinal force information, because the longitudinal force in rail due to temperature change is still difficult to be accurately measured [28].

Furthermore, a target area can be much smaller rather than the whole half surface, and then the damage can be localized within a smaller EPC part. Usually, a roughly wide target area is chosen to search for damage scope, and then a smaller target area is used to localize a particular damage.

This PIV analysis method has the potential to be applied to the monitoring of EPC deformation in the breathing zone of CWR, where the rail would move under the longitudinal force produced by temperature rising and falling.

3.3. Deformation of EPC from the side views

The rail in this experiment can be treated as a rigid body. Due to the irregular shape of rail cross section, the deformation of EPC in the cross section would be irregular.

In Fig. 11, the points G, M, E and K would undergo the same displacement with the rail movement since the rail can be treated as being rigid in comparison to EPC. Then it comes

$$G\bar{G}_1 = M\bar{M}_1 = E\bar{E}_1 = K\bar{K}_1 = D \tag{4}$$

From the geometry in Fig. 11,

$$\tan\alpha = \frac{G\bar{G}_1}{\bar{G}C} \tag{5}$$

$$\tan\beta = \frac{M\bar{M}_1}{\bar{M}N} \tag{6}$$

$$\tan\gamma = \frac{E\bar{E}_1}{\bar{E}B} \tag{7}$$

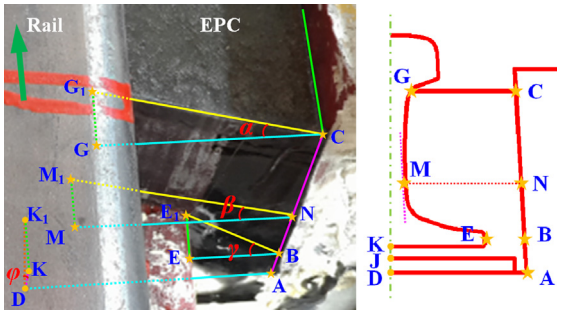

Fig. 11. Geometry in the cross section.

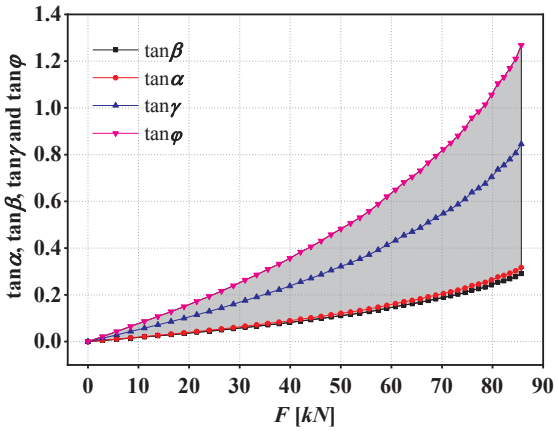

Fig. 12. Shear deformation of EPC among cross section.

$$\tan\varphi = \frac{K\bar{K}_1}{D\bar{K}} \tag{8}$$

where$\bar{GC}$ = 88 mm, $\bar{MN}$ = 96 mm, $\bar{BE}$ = 33 mm, and the thickness of rubber strip $\bar{DJ}$ is 12 mm. The vertical distance $\bar{JK}$ from the bottom of rail to the upper surface of the rubber strip depends on rail line levelling in construction. In this experiment, $\bar{JK}$ was 10 mm.

Then we can get the shear deformation of EPC within the cross section, as is shown in Fig. 12.

If there is no damage in the EPC itself, the shear deformation of EPC would be continuous, and then the shear deformation could be limited in the range between the pink solid triangle line and the black solid square line (the grey area in Fig. 12).

From Fig. 11 and Fig. 12, it can be understood that the vulnerable part of ERS is not only the EPC near the rail foot but also the EPC right under the rail, and especially the rubber strip, because these parts sustain even larger shear deformation than that at the rail foot.

Usually, the rubber strip is softer than EPC, and then the shear deformation of the rubber strip would be larger than that of EPC right under the rail. So the interface between the rubber strip and concrete groove would face the primary challenge in the push experiment.

It is verified from the observation in the experiment that the first debonding indeed happened right at the interface between the rubber strip and concrete groove, as shown in Fig. 13.

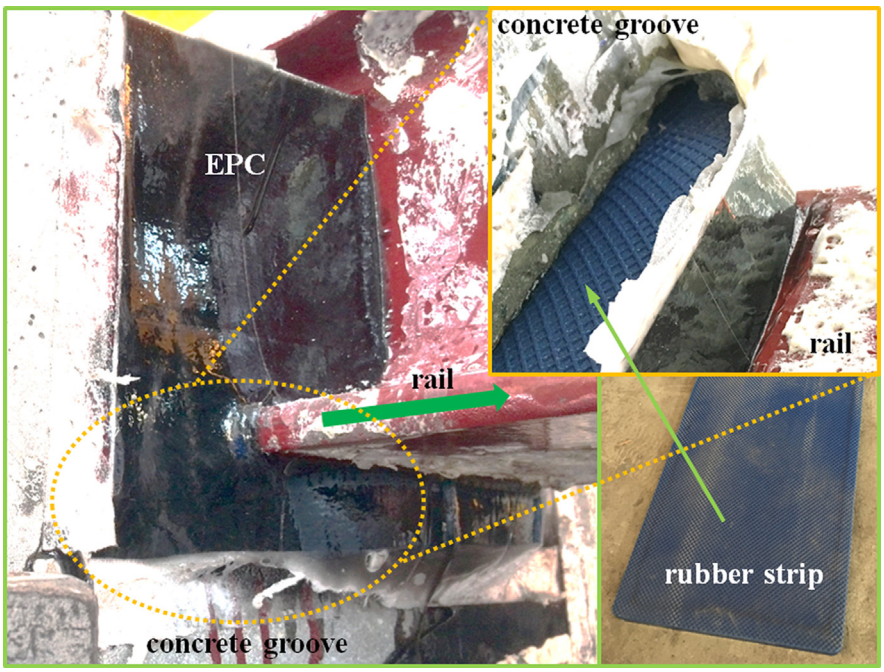

Fig. 13. First debonding at the interface between the rubber strip and the concrete groove.

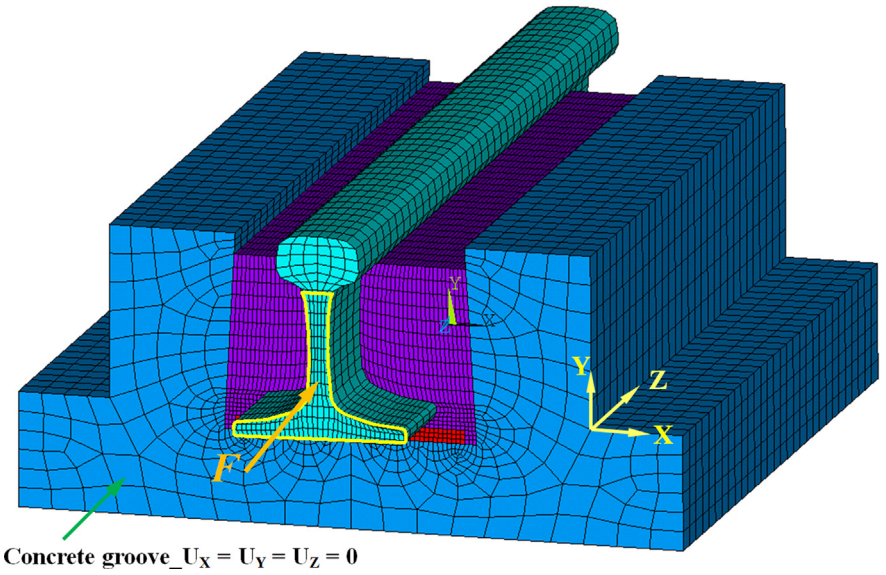

Fig. 14. FEA model of specimen.

Table 1
Material properties of components in ERS.

components	elastic modulus [MPa]	Poisson ratio	Density [kg/m^3]
rail	2.06E5	0.3	7800
EPC	6	0.495	1000
rubber strip	0.7	0.45	600
concrete groove	3.6E4	0.2	2400

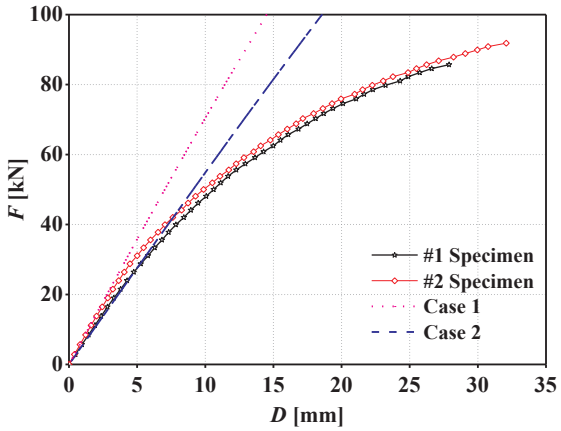

Fig. 15. Force-displacement curves: simulation results and experiment results.

4. Numerical analysis

4.1. Finite element ERS model

To better understand the damage initiation and growth process, a finite element analysis (FEA) model is established, as shown in Fig. 14.

In the FEA model, the concrete groove is fixed with no displacement in x, y or z direction and the rail is pushed at rail web and rail foot. EPC and the rubber strip should be hyperelastic. In this qualitative analysis, EPC and rubber strip are all presumed to be linear elastic and their elastic modulus and Poisson's ratios thus could be acquired from simple tension tests [29]. The material properties of the components of the ERS used for the numerical analysis are listed in table 1.

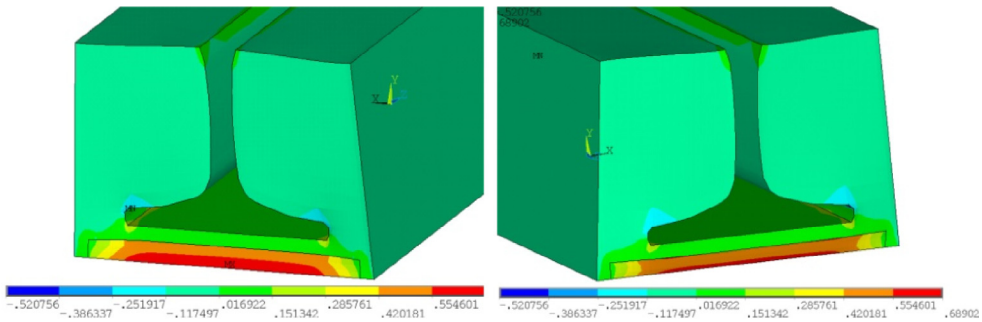

(a) YZ shear strain at push end in Case 1 (b) YZ shear strain at free end in Case 1

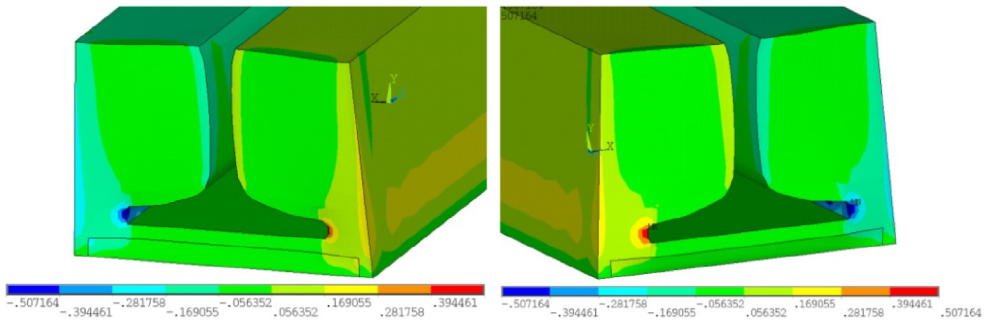

(c) XZ shear strain at push end in Case 1 (d) XZ shear strain at free end in Case 1

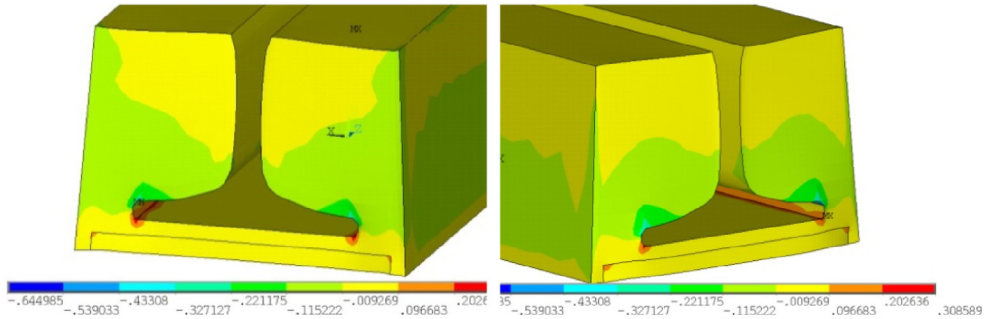

(e) YZ shear strain at push end in Case 2 (f) YZ shear strain at free end in Case 2

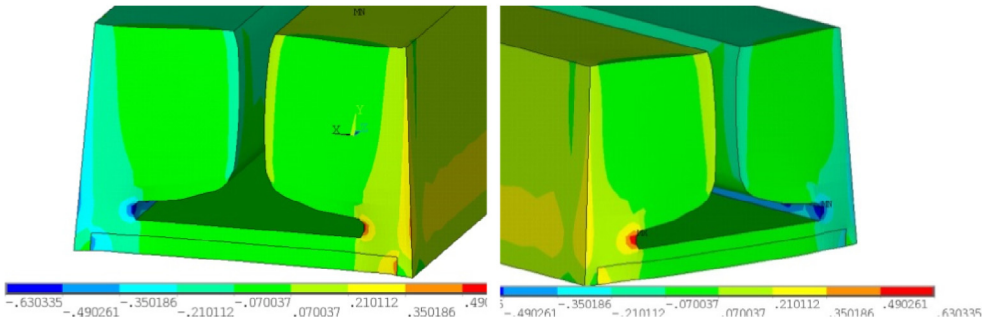

(g) XZ shear strain at push end in Case 2 (h) XZ shear strain at free end in Case 2

Fig. 16. YZ shear strain and XZ shear strain (F = 60 kN).

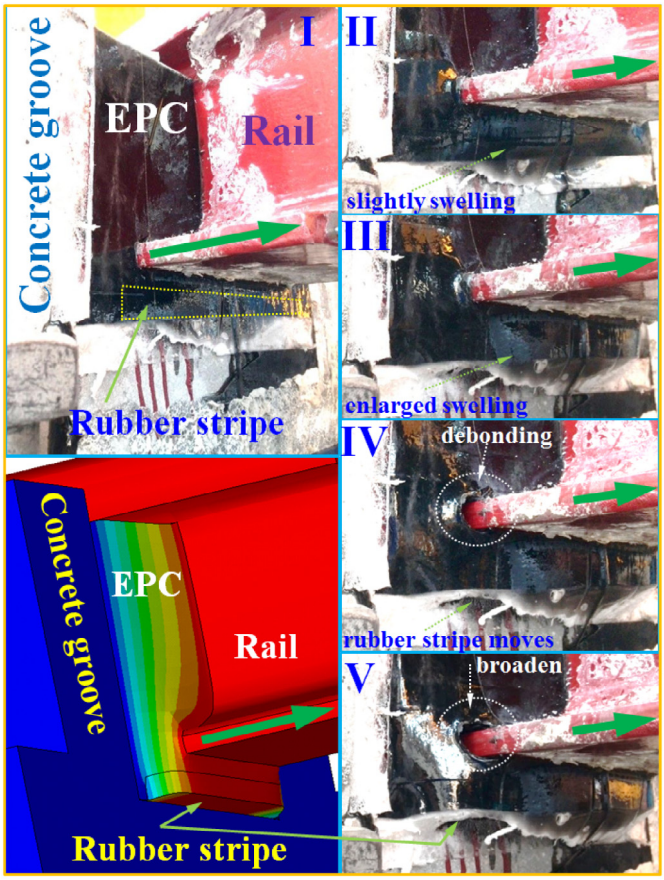

(a) free end

(I. original state; II. at the location of rubber stripe, it appears slight swelling; III. enlarged swelling; IV. debonding happened at the rail foot, and the rubber stripe moved; V. debonding broadened)

Fig. 17. Damage initiation and growth from experiment observations.

In the simulation, two cases are considered.

Case 1: the rubber strip never debonds from concrete groove;

Case 2: the rubber strip is not glued to the concrete groove but friction exists between them with a friction coefficient of 0.8 [30–31].

4.2. Numerical analysis to explain experimental results

The force–displacement curves obtained from the simulation are almost linear and only bending slightly, as illustrated in Fig. 15.

The bond between the rubber strip and the concrete groove makes the longitudinal resistance stronger, so the gradient of pink dot line (Case 1) is larger than that of blue dash line (Case 2).

In the beginning of the experiment, the rubber strip and the concrete groove stuck with each other very well. When the shear deformation of rubber strip was large enough, the rubber strip began to debond from the concrete groove. That is why the black open star line (#1 Specimen) and red open diamond line (#2 Specimen) are between the pink dot line (Case 1) and blue dash line (Case 2) in the displacement range from 0 to about 5 mm.

The difference between the simulation results and the experimental results comes from two factors. One is the material property consideration. As mentioned above, in the simulation, EPC and rubber strip are all considered as linear elastic materials. But actually, they are hyperelastic materials with nonlineaity. The other factor is the cracking or debonding happening in ERS.

Fig. 16 shows the YZ and XZ shear strains in the simulation when the applied force is 60 kN.

It can be seen from Fig. 16 that, the rubber strip bears the largest YZ strain in Case 1 (Fig. 16(a) ~ Fig. 16(d)), up to 68.9%,

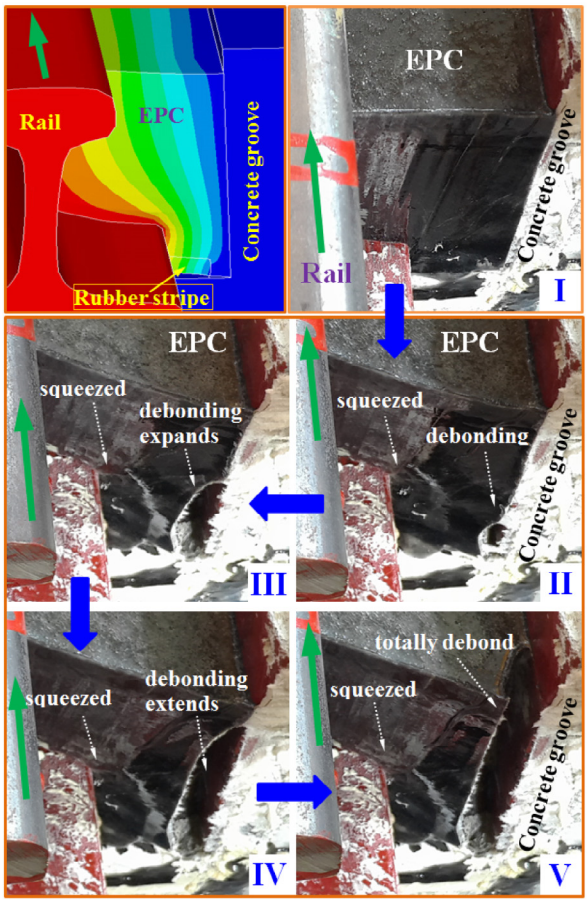

(b) push end

(I. original state; II. the EPC at the rail foot was squeezed due to friction, and at the interface between EPC and concrete groove, debonding appeared; III. the debonding expanded; IV. the debonding extented upward; V. EPC and concrete groove totally debonded from each other)

Fig. 17. (*continued*)

making the interface between the rubber stripe and the concrete groove the most dangerous place facing the primary challenge. While at the rail foot, both YZ strain and XZ strain appear intense, yet are slightly lower than the YZ strain at the rubber stripe.

When it comes to Case 2 (Fig. 16(e) ~ Fig. 16(h)), the rubber strip would not bear much YZ strain or XZ strain, because the debonding between rubber strip and concrete groove makes the shear strain of rubber strip release soon. In this case, rail foot becomes the most dangerous location where both the YZ strain and XZ strain are all so high, about 64.5% and 63.0% respectively.

From this qualitatively simulation, the damage initiation and growth of ERS under longitudinal force can be understood. It is most probably that debonding firstly takes place between the rubber strip and the concrete groove, and then comes to the rail foot between EPC and the rail. The debonding between rubber strip and concrete groove could slow down the debonding between EPC and the rail at the rail foot.

Fig. 17 shows the damage initiation and growth process at the free end and the push end in the experiments.

In Fig. 17(a), it is easy to see the debonding between the EPC and the rail at the rail foot at the free end (IV and V), but the movement of rubber strip should be observed carefully. Actually, before the debonding between the EPC and the rail, at the location of the rubber strip, it appeared swelling (see Fig. 17(a) II and III). Before long, part of the lower surface of the undamaged rubber strip can be seen from under the side view (see Fig. 13 and Fig. 17(a) III ~ V). Rubber strip moves with EPC and rail. At the interface between concrete groove and rubber strip, it is still unknown whether the concrete groove or the adhesive was damaged. Almost at the same time, the debonding between the EPC and the rail at the rail foot becomes more and more obvious, as shown in Fig. 17(a) IV and V.

At the push end, the situation was somewhat different. It is difficult to see the debonding between EPC and rail at the rail foot, where the EPC was squeezed, as shown in Fig. 17(b) II ~ V. Maybe debonding happened but possibly the friction held the EPC and the rail together at the rail foot. Then the interface between the EPC and the concrete groove became a vulnerable part. EPC debonded from concrete groove along their interface from bottom to top, as shown in Fig. 17(b). The condition in Fig. 17(b) V was when the experiment stopped.

5. Conclusions and future work

In this research, the damage development in ERS under longitudinal force was investigated both experimentally and numerically. From the analysis, the conclusions and the work need to do in the near future are as follows:

(1) The damage evolution of ERS under longitudinal force could be divided into three stages: linear elasticity, damage initiation and damage acceleration stages. In the future, a method to detect cracks and debonds at the interfaces and inside EPC in ERS will be developed in order to confirm that this three stages indeed exist. This method can also be the basis for nondestructive detection of early stage damage of ERS in real railway track. Hammer test [32] and axle box acceleration measurement [33–34] have the potential to be candidates of this kind of methods.
(2) PIV method is capable of providing accurate and high quality measurement of the surface deformation of EPC. The damage can be localized within a small EPC part. Further statistical analysis shows that the percentage distribution of the absolute displacements of the interrogation areas changes in agreement with the rail displacement increment rather than its gradient (by force), benefit from which, damage assessment is possible to be conducted in the absence of longitudinal force information. This PIV analysis method will be tested for monitoring of EPC deformation in breathing zone of CWR.
(3) The analysis of the deformation of EPC from side views reveals that the damage initiation and growth process are determined by the large shear strain of rubber strip and intense shear strain of EPC at rail foot. This is verified by the qualitative analysis with finite element method. Thus, the shear strengths of EPC, rubber strip and the adhesives at the interfaces should be as strong as possible.
(4) The material properties of EPC and rubber strip are not investigated. Their constitutive relationships should be explored in order to make the simulation more accurate. Moreover, with the parameters of material strengths, the simulation of damage initiation and development path would be possible. Further research on material properties and strength parameters will possibly make the FEA from qualitatively to quantitatively.

Declaration of Competing Interest

The authors declare that they have no known competing financial interests or personal relationships that could have appeared to influence the work reported in this paper.

Acknowledgement

This research is supported by the open research fund of MOE Key Laboratory of High-speed Railway Engineering, Southwest Jiaotong University. Chengdu Xinzhu Corporation is gratefully acknowledged for preparing ERS specimens and other necessities for experiments. Also, the first author sincerely thanks the financial support from the China Scholarship Council.

References

[1] C. Esveld, Modern Railway Track (2nd Edition)[M], Elsevier, Delft, 2001, pp. 253–264.
[2] Brochures from edilon)(sedra[DB/OL]. https://www.edilonsedra.com/downloads/.
[3] V. Markine, A. De Man, S. Jovanovic, et al., Modelling and optimization of an embedded rail structure[J], Rail International 31 (7) (2000) 15–23.
[4] S.G. Li, J. Wu, R.H. Petrov, et al., "Brown etching layer": A possible new insight into the crack initiation of rolling contact fatigue in rail steels?[J], Eng. Fail. Anal. 66 (2016) 8–18.
[5] F.J. Franklin, A. Kapoor, Modelling wear and crack initiation in rails [J], Proceedings of the Institution of Mechanical Engineers, Part F: Journal of Rail and Rapid Transit 221 (1) (2007) 23–33.
[6] Y. Zhou, Y.B. Han, D.S. Mu, et al., Prediction of the coexistence of rail head check initiation and wear growth [J], Int. J. Fatigue 112 (2018) 289–300.
[7] H. Zhu, H. Li, A. Al-Juboori, et al., Understanding and treatment of squat defects in a railway network [J], Wear, Volumes 442–443 (2020) 203139.
[8] M.J. Buehler, F.F. Abraham, H.J. Gao, Hyperelasticity governs dynamic fracture at a critical length scale[J], Nature 426 (13) (2003) 141–146.
[9] M.J. Buehler, H.J. Gao, Dynamical fracture instabilities due to local hyperelasticity at crack tips[J], Nature 439 (7074) (2006) 307–310.
[10] M.F. Kaplan, Crack propagation and the fracture concrete[J], ACI Journal Proceedings 58 (11) (1961) 591–610.
[11] Z.P. Bazant, Concrete fracture models: testing and practice [J], Eng. Fract. Mech. 69 (2002) 165–205.
[12] B. Goszczynska, Analysis of the process of crack initiation and evolution in concrete with acoustic emission testing [J], Archives of Civil and Mechanical Engineering 14 (2014) 134–143.
[13] A.H. Muhr, A.G. Thomas, J.K. Varkey, A fracture mechanics study of natural rubber-to-metal bond failure[J], J. Adhes. Sci. Technol. 10 (7) (1996) 593–616.
[14] I. Grant, Particle image velocimetry: A review[J], Proceedings of the Institution of Mechanical Engineers, Part C: Journal of Mechanical Engineering Science 211 (1) (1997) 55–76.
[15] A.S. Michael, O. Jean-Jose, S. Hubert, Image Correlation for Shape, Motion and Deformation Measurements - Basic Concepts, Theory and Applications[M], Springer, New York, 2009.
[16] D. Garcia, A fast all-in-one method for automated post-processing of PIV data[J], Exp. Fluids 50 (2011) 1247–1259.
[17] S.A. Stanier, J. Blaber, W.A. Take, et al., Improved image-based deformation measurement for geotechnical applications [J], Can. Geotech. J. 53 (5) (2016) 727–739.

[18] L.C.S. Nunes, D.C. Moreira, Simple shear under large deformation: Experimental and theoretical analyses[J], Eur. J. Mech. A. Solids 42 (2013) 315–322.
[19] D.C. Moreira, L.C.S. Nunes, Comparison of simple and pure shear for an incompressible isotropic hyperelastic material under large deformation[J], Polym. Test. 32 (2) (2013) 240–248.
[20] L.C.S. Nunes, Shear modulus estimation of the polymer polydimethylsiloxane (PDMS) using digital image correlation[J], Mater. Des. 31 (1) (2010) 583–588.
[21] J.L. Xiao, H. Liu, G.Z. Liu, et al., Study on characteristics and law of longitudinal resistance hysteretic curves of ballast bed of high-speed railway[J], Journal of the China Railway Society 40 (2) (2018) 91–99.
[22] H.F. Li, M. Yoda, Multilayer nano-particle image velocimetry (MnPIV) in microscale Poiseuille flows[J], Meas. Sci. Technol. 19 (2008) 1–9.
[23] Y.U. Min, K.C. Kim, Hybrid micro-/nano-particle image velocimetry for 3D3C multi-scale velocity field measurement in microfluidics[J], Meas. Sci. Technol. 22 (2011) 1–12.
[24] Sveen, J. K., 2004. An introduction to MatPIV v. 1.6.1. eprint series, Dept. of Math. University of Oslo NO. 2 ISSN 0809-4403. (https://www.mn.uio.no/math/english/people/aca/jks/matpiv/).
[25] Z.J. Taylor, R. Gurka, G.A. Kopp, et, al. Long-duration time-resolved piv to study unsteady aerodynamics[J]. Instrumentation and Measurement, IEEE Transactions, 2010, 59(12): 3262-3269. (https://ieeexplore.ieee.org/stamp/stamp.jsp?tp=&arnumber=5464317&isnumber=5609237&tag=1).
[26] W. Thielicke, E.J. Stamhui, PIVlab – Towards User-friendly, Affordable and Accurate Digital Particle Image Velocimetry in MATLAB[J], Journal of Open Research Software 2 (1) (2014) 1–10.
[27] W. Thielicke, E.J. Stamhui. PIVlab - Time-Resolved Digital Particle Image Velocimetry Tool for MATLAB (version: 1.43). 2014.
[28] P. Wang, K.Z. Xie, L.Y. Shao, L.S. Yan, et al., Longitudinal force measurement in continuous welded rail with bi-directional FBG strain sensors [J], Smart Mater. Struct. 25 (1) (2015) 1–10.
[29] Alan N. Gent, Engineering with rubber: how to design rubber components, 3rd edition, Hanser Publications, Cincinnati, USA, 2012.
[30] Engineering ToolBox, (2004). Friction and Friction Coefficients. [online] Available at: https://www.engineeringtoolbox.com/friction-coefficients-d_778.html.
[31] E.H. Bani-Hani, J. Lopez, G. Mohanan, Data on the coefficient of static friction between surfaces coated with different sizes of rubber granules produced from used tires[J], Data in Brief 22 (2019) 940–945.
[32] M. Oregui, Z. Li, R. Dollevoet, Identification of characteristic frequencies of damaged railway tracks using field hammer test measurements[J], Mech. Syst. Sig. Process. 54–55 (2015) 224–242.
[33] M. Molodova, Z. Li, R. Dollevoet, Axle box acceleration: Measurement and simulation for detection of short track defects[J], Wear 271 (1–2) (2011) 349–356.
[34] M. Oregui, S. Li, A. Núñez, Z. Li, R. Carroll, R. Dollevoet, Monitoring bolt tightness of rail joints using axle box acceleration measurements[J], Structural Control And Health Monitoring 24 (2) (2016) 1–15.